Modeling and Analysis of AC Output Power Factor for Wireless Chargers in Electric Vehicles

Xi Zhang, *Senior Member, IEEE*, Tianze Kan, *Student Member, IEEE*, Chenwen You, and Chris Mi, *Fellow, IEEE*

***Abstract*—This paper presents a general mathematical expression and characteristic analysis of the output power factor before rectification on the receiver side for wireless chargers in electric vehicles. This power factor is usually regarded as unity (i.e., the ac output voltage is in phase with the current), based on fundamental harmonic approximation. However, the default unity power factor assumption is not accurate for output power derivation even at resonance frequency. This study explores not only output power factor characteristics for different frequencies or power levels, but also the phase relationships of the input and output ac voltages. The continuous conduction mode and discontinuous conduction mode are both analyzed. An integrated *LCC* compensation topology is selected as the research object, and its analysis process can be readily extended to other common topologies. Furthermore, this study is beneficial for the implementation of some control strategies requiring precise power computation/estimation, e.g., feedforward control or model prediction control. Finally, a comparison of numerical and experimental results with various misalignment cases validates correctness of the proposed theoretical derivation and analysis methodology.**

***Index Terms*—Continuous conduction mode (CCM), discontinuous conduction mode (DCM), electric vehicle, power factor, wireless charger.**

I. Introduction

In recent years, the keen attention being paid to transportation electrification and the rising deployment of electric vehicles (EVs) have made it essential for researchers, enterprises, and governments to deal with several barriers to the wide acceptance of EVs, including inconvenience of charging, unsatisfactory driving distance, relatively high cost, and so on [1], [2]. Wireless power transfer (WPT) technology is an effective approach to address the first problem of inconvenient charging, due to the fact that it removes the need for cables or plugs, galvanic isolation of on-board electronics and additional safety concerns with operating in rain and snow [3]–[5]. Thus, it offers consumers a seamless and convenient alternative for charging efficiently. Till now, there has been considerable literature focusing on the application of WPT technology in real wireless charging systems for electric vehicles on the road. Magnetic coupler design, compensation topologies, foreign object detection, effective control strategies, and so on are the major aspects of this technology [6]–[11].

A typical WPT system includes several stages, such as a rectifier with power factor correction, an inverter, a compensation network on the transmitter side, a magnetic coupler (including the transmitter and receiver coils), a compensation network on the receiver side, and a rectifier for charging the dc battery [12], [13]. A dc–dc converter may be added between the rectifier and inverter on the transmitter side for input dc voltage adjustment. Four basic compensation topologies are labeled as series–series (SS), series–parallel (SP), parallel–series (PS), and parallel–parallel (PP), according to the way the capacitors are connected to the transmitter and receiver coils [14]–[17]. Some other novel compensation topologies have been proposed recently. In [18], a series–parallel–series (SPS) compensation topology is presented. In this new design, one capacitor is connected in series, while the other is connected in parallel with the transmitter coil. On the receiver side, one capacitor is connected in series with the coil. Thus, both SS and PS characteristics appear in the topology. An *LCL* network is proposed in [19], where the transmitter is featured as a constant current source. In [20], an SP *LCC* compensation is used for better performance, despite its tricky parameter design needed for control stability and soft-switching realization. An integrated *LCC* compensation is proposed to reduce the size and weight of additional inductors in [21]. Thrimawithana and Madawala [22] introduced a *CLCL* network where bidirectional power transfer can be achieved.

All the aforementioned topologies were analyzed under resonance condition at the resonant frequency. In such a case, when the input and output voltages are fixed, the output power is regarded as constant. However, in practical charging systems, a low power requirement is sometimes raised for recovery charging when SOC approaches its upper limit [23]–[25]. Therefore, modulation of the input dc voltage or inverter switching frequency is also necessary. Frequency modulation is an effective approach if the input dc voltage cannot be adjusted when there is no dc–dc converter between the input rectifier and inverter. Although phase shift modulation is also a useful scheme for power adjustment of a WPT system, sometimes the power cannot be adjusted to even higher despite of phase shift modulation at a fixed frequency, so in this case, frequency modulation might be more effective for higher power derivation. Nevertheless, to authors' best knowledge, the characteristics of power, phase, and efficiency are still unclear for various frequencies or misalignments. Therefore, precise theoretical analysis is necessary as frequency modulation guidance in engineering applications to obtain a wider power range. In this paper, operations at various

Manuscript received November 8, 2015; revised January 13, 2016 and February 13, 2016; accepted March 7, 2016. Date of publication March 15, 2016; date of current version November 11, 2016. This work was supported by the National Natural Science Foundation of China (NSFC) under Grant 51277121. Recommended for publication by Associate Editor S.-C. Tan.

X. Zhang is with the School of Mechanical Engineering, Shanghai Jiao Tong University, Shanghai 200240, China (e-mail: braver1980@sjtu.edu.cn).

T. Kan, C. You, and C. Mi are with the Department of Electrical and Computer Engineering, San Diego State University, San Diego, CA 92182 USA (e-mail: bigtreehust@gmail.com; chenwyou90@gmail.com; mi3032@ gmail.com).

Color versions of one or more of the figures in this paper are available online at http://ieeexplore.ieee.org.

Digital Object Identifier 10.1109/TPEL.2016.2542163

frequencies other than the resonant frequency are considered and discussed. In addition, in the aforementioned proposals, the ac output of the compensation network on the receiver side was always regarded to possess unity power factor, since the authors thought the ac output voltage to be in phase with the output current, due to the conduction mode of the diodes in the rectifier; however, this description is not accurate because the actual output current is not in the shape of an ideal sinusoidal waveform and the phase difference between the output current and voltage cannot be ignored. If the output power factor is not considered, the theoretical output power is usually calculated to be significantly greater than the value measured by a power analyzer.

Reliable acquisition of output power factor via thorough theoretical derivation is beneficial for the implementation of several control algorithms (e.g., feedforward control, model prediction control, etc.), which require real-time precise estimation of output power, supposing the input and output voltages and switching frequency are known. On the other hand, the exploration of voltage/current phase relationships and power analysis at various frequencies could make contributions to the design of a novel compensation topology. Therefore, this study is meaningful to the development of effective control strategies in WPT systems and circuit design as well.

An *LCL* converter can be formed by adding an *LC* compensation network on the primary side or on both primary (transmitter) and secondary (receiver) sides. The advantage for the *LCL* converter at the resonant frequency is that the current in the primary-side coil can be independent of the load condition, or in other words, the *LCL* network performs like a current source. However, the design of an *LCL* converter usually requires additional inductors. To reduce the additional inductor size and cost, usually a capacitor is put in series with the primary-side coil, which forms an *LCC* compensation network. By utilizing an *LCC* compensation network, a zero current switching condition could be achieved for higher efficiency by tuning the compensation network parameters. Also, when the LCC compensation network is adopted at the secondary side, the reactive power at the secondary side could be somehow compensated and the current distortion might be reduced. Consequently, in order to verify the proposed theoretical derivation, an integrated *LCC* compensation topology is selected as a specific research object. Extension of the presented analysis to other topologies is based on simple transformation rules. A brief description of the integrated *LCC* compensation topology is given in Section II. A general mathematical modeling that considers variation of frequencies is depicted in Section III. Section IV provides the detailed theoretical derivation of ac output power factor and voltage phase relationships for continuous conduction mode (CCM) and discontinuous conduction mode (DCM). Experimental and numerical results are compared in Section V. This is followed by conclusions in Section VI.

II. Studied WPT System Topology

An integrated *LCC* compensation topology, shown in Fig. 1, is selected as the research object for the explanation of the proposed theory. The transmitter side is comprised of a high-frequency inverter, an *LCC* compensation network and a transmitter coil. The compensation network—C_1, C_{f1}, L_{f1}, and the coil L_1—constitutes a compensation resonant circuit. The inverter with full bridge structure is composed of four power MOSFETS ($S_1 \sim S_4$). The receiver side consists of a symmetrical *LCC* compensation resonant circuit and a rectifier. For the purpose of battery pack charging, an *LC* filter network is placed on the receiver side. As shown in Fig. 1, the main coil and the additional coil on the same side are coupled for size reduction. The mutual inductances of L_{f1}/L_1, L_{f2}/L_2, and L_1/L_2 are M_1, M_2, and M, respectively.

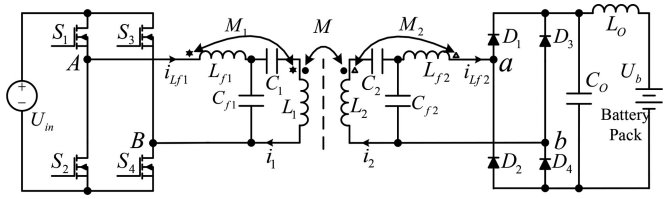

Fig. 1. Studied integrated *LCC* compensation topology.

When the electric vehicle experiences different ground clearance or misalignment conditions, the mutual inductance M between the two main coils will vary accordingly, while the other two mutual inductances between the main and additional coils, M_1 and M_2, remain constant. Due to the fact that a large leakage inductance exists and only mutual inductance contributes to the power transfer, a series capacitor should be added to compensate for the self-inductance.

The output voltage of the inverter is a square ac waveform, which consists of a fundamental component and higher odd order harmonics. To simplify the analysis of the *LCC* compensation topology at a single frequency, the inverter output voltage is regarded as sinusoidal. The decoupled circuit and simplified equivalent circuit models are given at an angular frequency of ω (not only resonance frequency) in Fig. 2 (a) and (b), respectively.

III. General Mathematical Modeling

In the simplified equivalent circuit model, the topology changes to a simple resonant *LCL* converter, as shown in Fig. 2 (b). The equivalent parameters can be expressed using real physical parameters as follows:

$$L_{f1e} = L_{f1} + M_1 \tag{1}$$

$$L_{f2e} = L_{f2} + M_2 \tag{2}$$

$$L_{e1} = L_1 + M_1 - 1/(\omega^2 C_1) \tag{3}$$

$$L_{e2} = L_2 + M_2 - 1/(\omega^2 C_2) \tag{4}$$

$$C_{f1e} = C_{f1}/(\omega^2 M_1 C_{f1} + 1) \tag{5}$$

$$C_{f2e} = C_{f2}/(\omega^2 M_2 C_{f2} + 1). \tag{6}$$

The circuit on the transmitter side is analyzed first. Based on Kirchhoff's current law, the input ac current is simply as

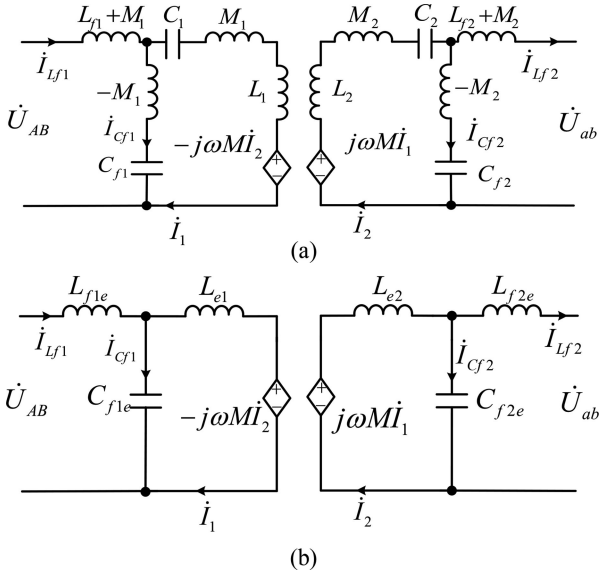

Fig. 2. Equivalent circuits. (a) Decoupled circuit model. (b) Simplified equivalent circuit model.

follows:

$$\dot{I}_{\mathrm{Lf1}} = \dot{I}_1 + \dot{I}_{\mathrm{Cf1}}. \tag{7}$$

The aforementioned equation can be rewritten using relevant voltages and impedances

$$\frac{\dot{U}_{\mathrm{AB}} - \dot{U}_{\mathrm{Cf1e}}}{j\omega L_{f1e}} = \dot{I}_1 + j\omega C_{f1e}\dot{U}_{\mathrm{Cf1e}}. \tag{8}$$

Consequently

$$\dot{U}_{\mathrm{Cf1e}} = \frac{\omega L_{f1e}\dot{I}_1}{j(1-\omega^2 L_{f1e}C_{f1e})} + \frac{\dot{U}_{\mathrm{AB}}}{1-\omega^2 L_{f1e}C_{f1e}}. \tag{9}$$

Kirchhoff's voltage law provides

$$\dot{I}_1 = \frac{\dot{U}_{\mathrm{Cf1e}} + j\omega M\dot{I}_2}{j\omega L_{e1}}. \tag{10}$$

Thus, substitute (9) into (10) and let $a_1 = 1-\omega^2 L_{f1e}C_{f1e}$, and one can derive the following expression for the current going across the main coil:

$$\dot{I}_1 = \frac{\dot{U}_{\mathrm{AB}}}{j\omega(L_{e1}a_1 + L_{f1e})} + \frac{Ma_1\dot{I}_2}{L_{e1}a_1 + L_{f1e}}. \tag{11}$$

Similarly, the circuit equations on the receiver side can be described as follows:

$$\dot{U}_{\mathrm{Cf2e}} = \frac{\dot{U}_{\mathrm{ab}}}{a_2} - \frac{\omega L_{f2e}\dot{I}_2}{ja_2} \tag{12}$$

$$\dot{I}_2 = -\frac{\dot{U}_{\mathrm{ab}}}{j\omega(L_{e2}a_2 + L_{f2e})} + \frac{Ma_2\dot{I}_1}{L_{e2}a_2 + L_{f2e}} \tag{13}$$

where $a_2 = 1-\omega^2 L_{f2e}C_{f2e}$. For further simplification, we define $\sigma_1 = L_{e1}a_1 + L_{f1e}$ and $\sigma_2 = L_{e2}a_2 + L_{f2e}$, and (11) and (13) are then converted to the following expressions:

$$\dot{I}_1 = \frac{\dot{U}_{\mathrm{AB}}}{j\omega\sigma_1} + \frac{Ma_1\dot{I}_2}{\sigma_1} \tag{14}$$

$$\dot{I}_2 = -\frac{\dot{U}_{\mathrm{ab}}}{j\omega\sigma_2} + \frac{Ma_2\dot{I}_1}{\sigma_2}. \tag{15}$$

Supposing $\dot{I}_1$ and $\dot{I}_2$ are two "unknowns" in the equation set consisting of (14) and (15), the solution of the current of the main coil on the receiver side is depicted as

$$\dot{I}_2 = \frac{Ma_2}{j\omega(\sigma_1\sigma_2 - M^2a_1a_2)}\dot{U}_{\mathrm{AB}} - \frac{\sigma_1}{j\omega(\sigma_1\sigma_2 - M^2a_1a_2)}\dot{U}_{\mathrm{ab}}. \tag{16}$$

Let $\delta = \sigma_1\sigma_2 - M^2a_1a_2$, and $\dot{I}_2$ is finally simplified as

$$\dot{I}_2 = \frac{Ma_2}{j\omega\delta}\dot{U}_{\mathrm{AB}} - \frac{\sigma_1}{j\omega\delta}\dot{U}_{\mathrm{ab}}. \tag{17}$$

Providing Kirchhoff's current law, it is simple to obtain

$$\dot{I}_{\mathrm{Lf2}} = \dot{I}_2 - \dot{I}_{\mathrm{Cf2}} = \dot{I}_2 - j\omega C_{f2e}\dot{U}_{\mathrm{Cf2e}}. \tag{18}$$

By substituting (17) into (18), we can get the following relationship among the output ac current and the input and output ac voltages:

$$\dot{I}_{\mathrm{Lf2}} = \frac{M}{j\omega\delta}\dot{U}_{\mathrm{AB}} - \frac{\sigma_1 - \omega^2\delta C_{f2e}}{j\omega\delta a_2}\dot{U}_{\mathrm{ab}}. \tag{19}$$

Therefore, the output current before the rectifier is finally delineated as follows:

$$\dot{I}_{\mathrm{Lf2}} = B(\omega)\dot{U}_{\mathrm{AB}}/j - A(\omega)\dot{U}_{\mathrm{ab}}/j \tag{20}$$

where $A(\omega) = \frac{\sigma_1 - \omega^2\delta C_{f2e}}{\omega\delta a_2}$ and $B(\omega) = \frac{M}{\omega\delta}$.

The integrated *LCC* resonant topology is transformed to a SS resonant topology by giving the following conditions: $L_{f1} = L_{f2} = M_1 = M_2 = C_{f1} = C_{f2} = 0$. Thus, (19) and (20) can be simplified to expressions for the relationships among the output current and input and output voltages in the SS topology. Similarly, the whole derivation process could also be simplified to be adaptive to the situation in the SS topology.

IV. Derivation of Power Factor Characteristics and Voltage Phase Relationship

The WPT system is deployed at a certain moment for charging a specific battery pack with fixed nominal voltage in an electric vehicle. Meanwhile, if the duty cycles of all MOSFETs in the inverter are set as constants, the WPT system will have a fixed output power with operation at the resonant frequency. However, sometimes lower power is required for charging recovery and battery lifetime extension. One effective way of achieving lower power is to change the switching frequency of the inverter. Thus, this study focuses on WPT operations with fixed input and output voltages at different frequencies around the resonant frequency.

If frequency changes dramatically, the resonant stage will likely vary. When diodes of the rectifier on the receiver side are all OFF, current cannot go through L_{f2} in the resonant circuit. In such a case, the resonant stage is called open stage (stage O).

When the instantaneous voltage between connection points *a* and *b* in Fig. 1, namely $U_{\rm ab}$, is lower than the battery voltage, diodes D_1 and D_4 (see Fig. 1) are OFF, while D_2 and D_3 are ON, and the resonance enters the negative clamped stage (stage N). On the contrary, when $U_{\rm ab}$ is greater than the battery voltage, the positive clamped stage (stage P) appears.

This study considers three operation modes at different frequencies, including CCM, DCM, and cutoff mode (CUTOFF). As long as there is a combination of stage O and a clamped stage (stage N or P), the WPT system operates in DCM. If only a clamped stage (stage P and/or N) exists, the operation should be in CCM. If no current passes through L_{f2} all the time, the mode is CUTOFF with stage O only. The analysis of output power factor and phase differences between input and output voltages cannot be the same in various operation modes. In mode CUTOFF, it is meaningless to analyze the power factor, since output current $i_{\rm Lf2}$ is always zero, so CUTOFF is not involved in such a discussion.

In CCM, the ac output voltage is a square waveform and the output current shares the same zero crossing points with the voltage. The Fourier fundamental component of the output voltage is in phase with it because of the characteristics of a square waveform. However, the output current waveform with Fourier series including various orders of harmonics is not symmetric or regular at all, which is totally different from the output voltage. So, the phase shift between the fundamental components of the output voltage and current exists. In DCM, the situation is much more complicated since the ac output voltage does not remain as a square waveform and the ac output current is not continuous any longer. Additionally, the part of the output voltage when the output current is zero in DCM does not contribute to the output power, so this part cannot be considered for power factor derivation. The phase difference between the ac output voltage and current in CCM might be visible due to the current distortions. However, it is sometimes not obviously visible especially at some operating frequencies in DCM, therefore, it cannot be guaranteed that the phase difference between the output voltage and current must exist. Consequently, it is necessary and meaningful to derive a general expression for the difference in phase of output voltage and current in both CCM and DCM. The following discusses the derivation of output power factor and voltage phase relationship in CCM and DCM, and attempts to find mathematical expressions for final output power of the WPT system, which is essential in some control systems where estimation of output power is required.

A. CCM

In CCM, the WPT system operation passes through the negative clamped stage (N) and positive clamped stage (P) in sequence, as shown in Fig. 3, so the instantaneous output voltage between points *a* and *b*, i.e., $u_{\rm ab}(t)$, is featured as a square waveform with fixed battery voltage on the receiver side. In addition, the instantaneous input voltage between points *A* and *B*, i.e., $u_{\rm AB}(t)$, is also a square waveform on the transmitter side, due to the pulsewidth modulation in the inverter. In Fig. 3, U_a and U_b stand for amplitudes of input and output voltages, respectively,

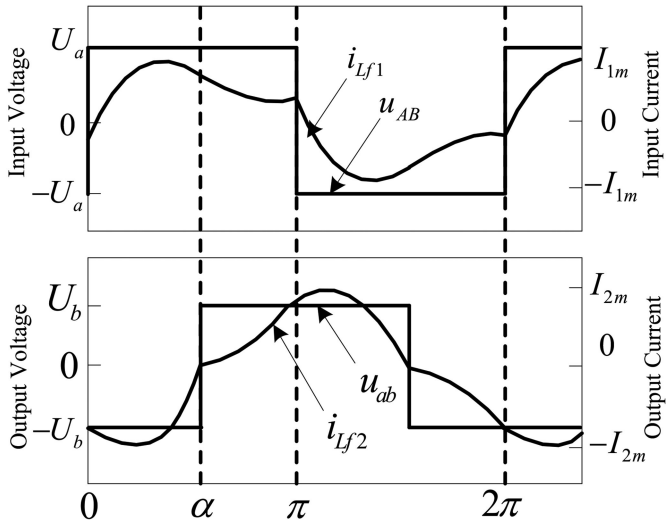

Fig. 3. Theoretical waveforms of CCM.

and I_{1m} and I_{2m} represent maximum values of input and output currents ($i_{\rm Lf1}(t)$ and $i_{\rm Lf2}(t)$), respectively. Thus, by using the Fourier transform, $u_{\rm AB}$ can be written as

$$u_{\rm AB}(t) = \frac{4}{\pi} U_a \sum_{n=1}^{+\infty} \frac{1}{2n-1} \sin[(2n-1)\omega t]. \tag{21}$$

It has to be noted that in real calculations, the upper limit of n is not infinite, but a predetermined natural number N. Similarly, let the phase difference between $u_{\rm AB}$ and $u_{\rm ab}$ be α, and $u_{\rm ab}$ can be expressed in the form of a Fourier series as

$$u_{\rm ab}(t) = \frac{4}{\pi} U_b \sum_{n=1}^{+\infty} \frac{1}{2n-1} \sin[(2n-1)(\omega t-\alpha)]. \tag{22}$$

Substitute (21) and (22) into (20), and we can obtain the Fourier series expression for the output current $i_{\rm Lf2}(t)$ as follows:

$$\begin{aligned} i_{\rm Lf2}(t) = & -\frac{4U_a}{\pi} \sum_{n=1}^{+\infty} \frac{1}{2n-1} B[(2n-1)\omega] \cos[(2n-1)\omega t] \\ & + \frac{4U_b}{\pi} \sum_{n=1}^{+\infty} \frac{1}{2n-1} A[(2n-1)\omega] \cos[(2n-1)(\omega t-\alpha)]. \end{aligned} \tag{23}$$

As seen in Fig. 3, when the system operation shifts from stage N to P or from stage P to N, $u_{\rm ab}$ experiences a rising edge from $-u_b$ to u_b or a falling edge from u_b to $-u_b$. In the meantime, $i_{\rm Lf2}$ changes its direction through the zero crossing point. So, at the instances $t = \alpha/\omega$ and $t = (\alpha+\pi)/\omega$, we have the following equations:

$$\begin{cases} i_{\rm Lf2}(\alpha/\omega) = 0 \\ i_{\rm Lf2}[(\alpha+\pi)/\omega] = 0. \end{cases} \tag{24}$$

A two-equation set is established for solving only one unknown α, which may cause some doubt. It is of no problem,

however, since when substituting $t = \alpha/\omega$ and $t = (\alpha + \pi)/\omega$ into (23), the following relationship exists:

$$i_{\mathrm{Lf2}}[(\alpha+\pi)/\omega] = -i_{\mathrm{Lf2}}(\alpha/\omega). \tag{25}$$

Consequently, the phase difference α between the input and output voltages can be definitively solved from the equation set (24). When solving the equation in practical operation, $B[(2n-1)\omega]$ is taken to be zero when n is greater than 1, since it drops in an exponential order and has a far smaller absolute value when $n > 1$ than when $n = 1$.

Due to the fact that the input and output voltages are in the form of square waveforms, their fundamental components in Fourier series should share the same phase difference, α. The fundamental component of the output ac current has a much greater amplitude than other high-order harmonics, and meanwhile, the ratio between the fundamental component and higher order harmonics of power, such as the magnification of current and voltage, is even greater than that of only the current. Therefore, the fundamental harmonic approximation (FHA) method is used for effective analysis of the output power factor of a WPT system. The fundamental component of the output current i_{Lf2} is derived from (23) as follows:

$$i_{\mathrm{Lf2,F}}(t) = \frac{4U_b}{\pi}A(\omega)\cos(\omega t-\alpha) - \frac{4U_a}{\pi}B(\omega)\cos(\omega t) \tag{26}$$

where the subscript F indicates the fundamental component. We define $C(\omega) = \frac{4U_b}{\pi}A(\omega)\sin(\alpha)$ and $D(\omega) = \frac{4U_a}{\pi}B(\omega) - \frac{4U_b}{\pi}A(\omega)\cos(\alpha)$, so (26) can be simplified as

$$i_{\mathrm{Lf2,F}}(t) = C(\omega)\sin(\omega t) - D(\omega)\cos(\omega t). \tag{27}$$

The aforementioned equation can be further written as a sinusoidal function

$$i_{\mathrm{Lf2,F}}(t) = E(\omega)\sin(\omega t-\beta) \tag{28}$$

where

$$E(\omega) = \sqrt{C^2(\omega)+D^2(\omega)} = \frac{4\sqrt{U_b^2A^2(\omega)+U_a^2B^2(\omega)-2U_aU_bA(\omega)B(\omega)\cos(\alpha)}}{\pi} \tag{29}$$

and

$$\tan(\beta) = \frac{D(\omega)}{C(\omega)} = \frac{B(\omega)U_a}{A(\omega)U_b}\csc(\alpha) - \cot(\alpha). \tag{30}$$

The fundamental components of the input and output voltages can be easily derived from (21) and (22) as follows:

$$u_{\mathrm{AB,F}}(t) = \frac{4U_a}{\pi}\sin(\omega t) \tag{31}$$

$$u_{\mathrm{ab,F}}(t) = \frac{4U_b}{\pi}\sin(\omega t-\alpha). \tag{32}$$

The phase difference between the output voltage $u_{\mathrm{ab,F}}$ and $i_{\mathrm{Lf2,F}}$ is $\varphi = \beta - \alpha$, so the ac output power factor $\lambda = \cos(\varphi) = \cos(\beta-\alpha)$. The input impedance $Z_{r,\mathrm{in}}$ before the rectifier on the receiver side can be calculated as

$$Z_{r,\mathrm{in}} = \frac{U_{\mathrm{ab,F}}}{I_{\mathrm{Lf2,F}}}\cos(\varphi) + j\frac{U_{\mathrm{ab,F}}}{I_{\mathrm{Lf2,F}}}\sin(\varphi) = \frac{4U_b\left[\cos(\varphi)+j\sin(\varphi)\right]}{\pi E(\omega)}. \tag{33}$$

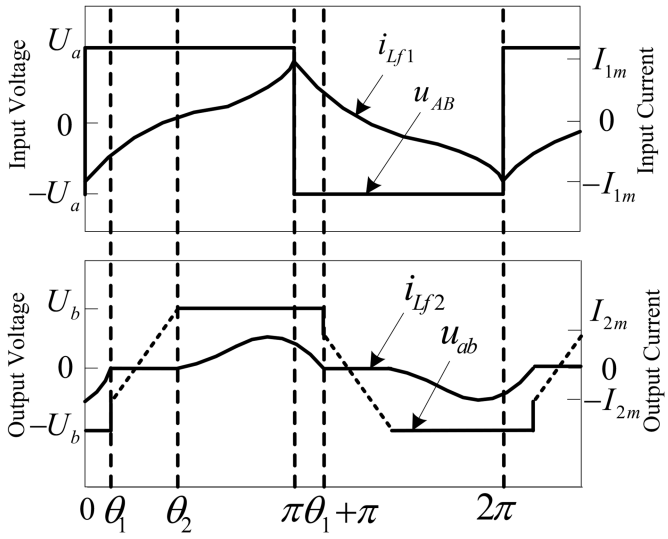

Fig. 4. Theoretical waveforms of DCM.

The output power before the rectifier could be calculated as

$$P_{\mathrm{CCM}}(\omega) = \frac{U_{\mathrm{ab,F}}I_{\mathrm{Lf2,F}}\lambda}{2} = \frac{2\lambda U_bE(\omega)}{\pi} = \frac{8\lambda U_b\sqrt{U_b^2A^2(\omega)+U_a^2B^2(\omega)-2U_aU_bA(\omega)B(\omega)\cos(\alpha)}}{\pi^2}. \tag{34}$$

Considering the loss of the rectifier, the actual output power to the battery is finally achieved using the following expression:

$$P_{\mathrm{out,CCM}} = P_{\mathrm{CCM}}(\omega) - P_{\mathrm{loss\_rectifier,CCM}}. \tag{35}$$

The loss of the rectifier $P_{\mathrm{loss\_rectifier,CCM}}$ is obtained based on the existing loss calculation equation for a four-diode uncontrolled rectifier with sinusoidal conduction current. It is easy to calculate the output power assuming the output dc voltage and current are known. However, in some control strategies, e.g., feedforward control or model prediction control, precise output power estimation is required, and measurements of output dc voltage and current do not help or are even not allowed. So, the aforementioned theoretical derivation of the output power considering interior parameter relationships in a topology is meaningful.

B. DCM

Unlike in CCM, stage O exists when the operation shifts from stage N to P or from P to N in DCM, meaning the output current, i_{Lf2}, stays at zero for a while between the negative and positive stage values, as shown in Fig. 4. The input voltage, u_{AB}, is kept as a square waveform after pulsewidth modulation of the

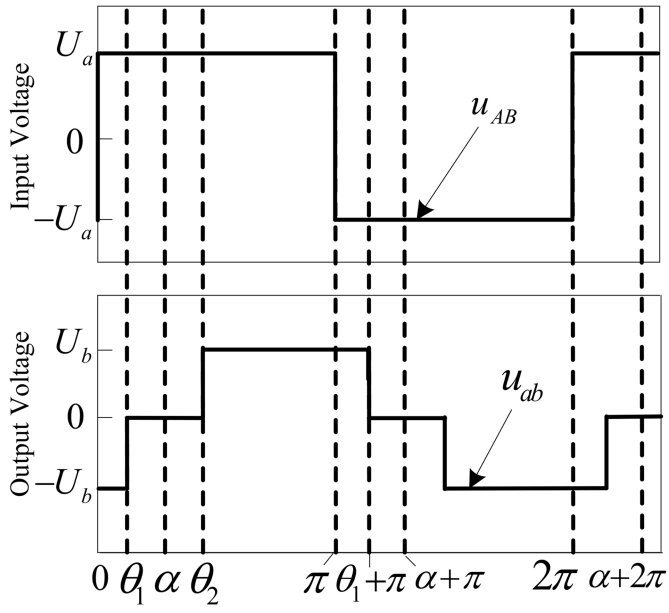

Fig. 5. Equivalent voltage waveforms of DCM.

inverter on the transmitter side; however, the output voltage, $u_{\rm ab}$, is not in the shape of a square waveform any longer due to the participation of stage O. The dashed lines used for the waveform of $u_{\rm ab}$ in Fig. 4 indicate that the value of $u_{\rm ab}$ in stage O is somehow uncertain in real situations, since the diode reverse recovery current and nonignorable $i_{\rm Lf2}$ slope may result in transient voltage oscillation of the rectifier input.

In order to acquire the Fourier transform of the output voltage with a difficulty output voltage Fourier transform due to uncertain shifting process with stage O, an equivalent waveform for the output voltage $u_{\rm ab}$ is proposed, where the voltage value can be "designed" to be zero in the shifting process, as seen in Fig. 5. This is because the output current, $i_{\rm Lf2}$, remains nearly zero and the variation of voltage does not contribute to the output power. In Figs. 4 and 5, θ_1 and θ_2, respectively, represent the starting and ending phases of stage O when output voltage increases. In Fig. 5, α stands for the midpoint of the shifting process, so $\alpha = \frac{\theta_1+\theta_2}{2}$. It is observed that the newly "designed" output voltage with one period from phase α to $\alpha+2\pi$ is an odd function for Fourier transform, so its fundamental component shares the same phase, α, relative to the phase zero of the input voltage, $u_{\rm AB}$.

The input voltage, $u_{\rm AB}$, is still in the shape of a square waveform, so its Fourier transform is given by

$$u_{\rm AB}(t) = \frac{4}{\pi}U_a \sum_{n=1}^{+\infty} \frac{1}{2n-1}\sin[(2n-1)\omega t]. \tag{36}$$

The output voltage, $u_{\rm ab}$, can be expressed as a general Fourier series expansion

$$u_{\rm ab}(t) = \sum_{n=1}^{+\infty} F(n)\sin[n(\omega t-\alpha)]. \tag{37}$$

Due to the symmetrical characteristics, it is only required to calculate the transformed function $F(n)$ of a half period. As seen in Fig. 4, the first half period from phase can be divided into two parts, i.e., stage O ($\alpha \sim \theta_2$ and $\theta_1+\pi \sim \alpha+\pi$) and stage P ($\theta_2 \sim \theta_1+\pi$). Thus, $F(n)$ is only contributed to by the effective part, i.e., stage P, and can be calculated as follows:

$$\begin{aligned} F(n) &= \frac{2}{\pi}U_b \int_{\phi}^{\pi-\phi} U_b \sin(n\omega t)d(\omega t) \\ &= \frac{2}{n\pi}U_b[\cos(n\phi)-\cos(n\pi-n\phi)] \end{aligned} \tag{38}$$

where $\phi = \theta_2-\alpha = \frac{\theta_2-\theta_1}{2}$. When n is even or odd, (38) output varies between zero and nonzero values, so the piecewise expression of $F(n)$ with even or odd n is given by

$$F(n) = \begin{cases} 0 & n = 2k \\ \frac{4U_b\cos(n\phi)}{n\pi} & n = 2k-1. \end{cases} \tag{39}$$

The final specific Fourier series expansion for the output voltage $u_{\rm ab}$ is depicted as

$$\begin{aligned} u_{\rm ab}(t) = &\frac{4}{\pi}U_b \sum_{n=1}^{+\infty} \frac{1}{2n-1}\cos[(2n-1)\phi] \\ &\times \sin[(2n-1)(\omega t-\alpha)]. \end{aligned} \tag{40}$$

The effective output current is determined by stage P, so the following piecewise expression exists

$$i_{\rm Lf2}(t) = \begin{cases} i_{\rm Lf2\_eff}(t) & \theta_2 \le \omega t \le \theta_1+\pi \\ 0 & \text{Otherwise.} \end{cases} \tag{41}$$

By substituting (36) and (41) into (20), we can obtain

$$\begin{aligned} i_{\rm Lf2\_eff}(t) = &-\frac{4U_a}{\pi}\sum_{n=1}^{+\infty}\frac{1}{2n-1}B[(2n-1)\omega]\cos[(2n-1)\omega t] \\ &+\frac{4U_b}{\pi}\sum_{n=1}^{+\infty}\frac{1}{2n-1}A[(2n-1)\omega]\cos[(2n-1)\phi] \\ &\times \cos[(2n-1)(\omega t-\alpha)]. \end{aligned} \tag{42}$$

At the end of stage P (phase $\theta_1+\pi = \alpha-\phi+\pi$), the output current $i_{\rm Lf2}$ drops to zero, so

$$i_{\rm Lf2\_eff}\left(\frac{\alpha-\phi+\pi}{\omega}\right) = 0. \tag{43}$$

In stage O, from $\alpha \sim \theta_2$, $\dot{I}_{\rm Lf2} = 0$, so according to (20), we have $\dot{U}_{\rm ab} = \frac{B(\omega)\dot{U}_{\rm AB}}{A(\omega)}$. Regardless of the uncertain interval in the newly "designed" waveform, the theoretical expression for output voltage $u_{\rm ab}$ in stage O is

$$u_{\rm ab\_O}(t) = \frac{4}{\pi}U_a\sum_{n=1}^{+\infty}\frac{B[(2n-1)\omega]}{(2n-1)A[(2n-1)\omega]}\sin[(2n-1)\omega t]. \tag{44}$$

At the end of the first stage O or the beginning of stage P (phase $\theta_2 = \alpha+\phi$), another condition provides

$$u_{\rm ab\_O}\left(\frac{\alpha+\phi}{\omega}\right) = U_b. \tag{45}$$

Consequently, (43) and (45) are composites of an equation set for solutions to two unknowns, α and ϕ.

Due to a reason similar to the one given in the CCM section, the FHA method is also used for effective analysis of the output power factor here. Using phase α as the starting point for Fourier transform over the period ($\alpha \sim \alpha + 2\pi$), the fundamental component of the output current, i_{Lf2}, is expressed as

$$i_{\mathrm{Lf2,F}}(t) = R(\omega)\sin(\omega t - \alpha) - S(\omega)\cos(\omega t - \alpha) \quad (46)$$

where the subscript F stands for the fundamental component. The coefficient of the sinusoidal function in (46) is derived from (41) as

$$\begin{aligned} R(\omega) &= \frac{2}{\pi}\int_{\phi}^{\pi-\phi} i_{\mathrm{Lf2\_eff}}\left(t+\frac{\alpha}{\omega}\right)\sin(\omega t)d(\omega t) \\ &= \xi(\omega) + \frac{4U_a}{\pi^2}\sum_{n=1}^{+\infty}\frac{U(n)}{2n+1}B\left[(2n+1)\omega\right] \end{aligned} \quad (47)$$

where

$$\xi(\omega) = \frac{4U_a B(\omega)\sin(\alpha)}{\pi^2}\left[\pi - 2\phi + \sin(2\phi)\right] \quad (48)$$

$$U(n) = \sin\left[(2n+1)\alpha\right]\left\{\frac{\sin(2n\phi)}{n} - \frac{\sin\left[2(n+1)\phi\right]}{n+1}\right\}. \quad (49)$$

The coefficient of the cosine functions in (46) is calculated as

$$\begin{aligned} S(\omega) &= -\frac{2}{\pi}\int_{\phi}^{\pi-\phi} i_{\mathrm{Lf2\_eff}}\left(t+\frac{\alpha}{\omega}\right)\cos(\omega t)d(\omega t) \\ &= \xi_1(\omega) + \frac{4}{\pi^2}\sum_{n=1}^{+\infty}\frac{V(n)A\left[(2n+1)\omega\right] - W(n)B\left[(2n+1)\omega\right]}{2n+1} \end{aligned} \quad (50)$$

where

$$\xi_1(\omega) = \frac{4}{\pi^2}\left[\sin(2\phi) - \pi + 2\phi\right]\left[U_b A(\omega)\cos(\phi) - U_a B(\omega)\cos(\alpha)\right] \quad (51)$$

$$V(n) = \cos\left[(2n+1)\phi\right]\left\{\frac{\sin(2n\phi)}{n} + \frac{\sin\left[2(n+1)\phi\right]}{n+1}\right\} \quad (52)$$

$$W(n) = \cos\left[(2n+1)\alpha\right]\left\{\frac{\sin(2n\phi)}{n} + \frac{\sin\left[2(n+1)\phi\right]}{n+1}\right\}. \quad (53)$$

Equation (46) can be further delineated as a pure sinusoidal function

$$i_{\mathrm{Lf2,F}}(t) = Q(\omega)\sin(\omega t - \alpha - \varphi) \quad (54)$$

where

$$Q(\omega) = \sqrt{R^2(\omega) + S^2(\omega)} \quad (55)$$

$$\tan(\varphi) = \frac{S(\omega)}{R(\omega)}. \quad (56)$$

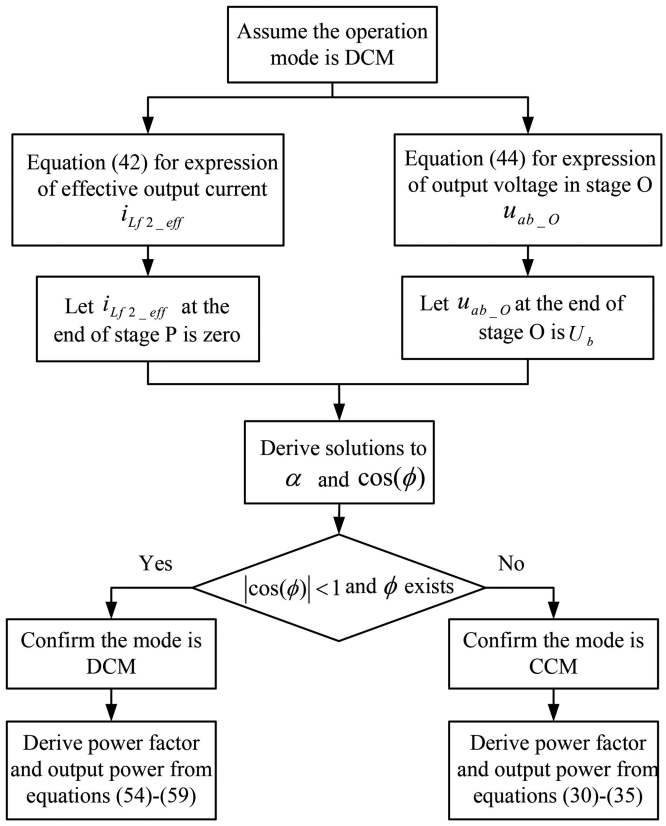

Fig. 6. Flow chart for mode identification and parameter derivation.

The input impedance $Z_{r,\mathrm{in}}$ before the rectifier on the receiver side can be calculated as

$$\begin{aligned} Z_{r,\mathrm{in}} &= \frac{U_{\mathrm{ab}}}{I_{\mathrm{Lf2}}}\cos(\varphi) + j\frac{U_{\mathrm{ab}}}{I_{\mathrm{Lf2}}}\sin(\varphi) \\ &= \frac{4U_b\cos(\phi)\left[\cos(\varphi) + j\sin(\varphi)\right]}{\pi Q(\omega)}. \end{aligned} \quad (57)$$

The ac output power factor is $\lambda = \cos(\varphi)$, so the output power before the rectifier is given by

$$P_{\mathrm{DCM}}(\omega) = \frac{U_{\mathrm{ab}} I_{\mathrm{Lf2}}\lambda}{2} = \frac{2\lambda U_b Q(\omega)\cos(\phi)}{\pi}. \quad (58)$$

Referring to (35), the actual output power to the battery, $P_{\mathrm{out,DCM}}$ for DCM is not difficult to compute, considering the loss of the rectifier, $P_{\mathrm{loss\_rectifier,DCM}}$, on the basis of the existing loss calculation equation for an uncontrolled four-diode rectifier. The expression for $P_{\mathrm{out,DCM}}$ is given by

$$P_{\mathrm{out,DCM}} = P_{\mathrm{DCM}}(\omega) - P_{\mathrm{loss\_rectifier,DCM}}. \quad (59)$$

C. Identification Conditions for CCM and DCM

If the system operation stays in CCM at a certain frequency, the output voltage shifts from N to P and from P to N in sequence without stage O. However, if the frequency goes to a lower or higher value, stage O appears, as well as DCM, and the phase difference between the starting and ending points (θ_1 and θ_2, shown in Figs. 4 and 5) is not zero any longer, due to the rising

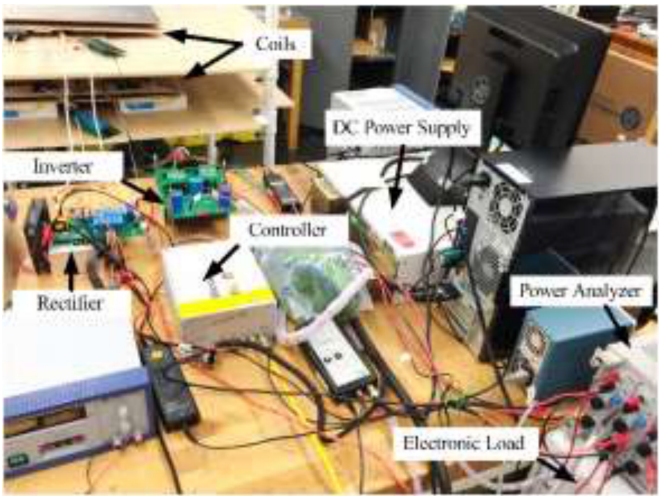

Fig. 7. Experimental setup for a WPT system.

TABLE I
SPECIFICATIONS OF THE WPT SYSTEM

Parameters	Value
Input dc voltage	250 V
Output dc voltage	250 V
X-misalignment tolerance	200 mm
Y-misalignment tolerance	150 mm
Switching frequency	76 kHz 104 kHz
Maximum power	1.5 kW
Maximum efficiency	94.3%
Transmitter coil inductance L_1	256 μH
Receiver coil inductance L_2	256 μH
Coupling coefficient of L_1 and L_1: k	0.12–0.28
Transmitter-side additional inductance L_{f1}	42.8 μH
Receiver-side additional inductance L_{f2}	39.4 μH
Mutual inductance between L_1 and L_{f1}: M_1	25.8 μH
Mutual inductance between L_2 and L_{f2}: M_2	25.2 μH
Transmitter-side series capacitance C_1	14.0 nF
Receiver-side series capacitance C_1	15.2 nF
Transmitter-side parallel capacitance C_{f1}	75.9 nF
Receiver-side parallel capacitance C_{f2}	75.9 nF

edge of the output voltage. So, $\phi = (\theta_2 - \theta_1)/2$ satisfies $\phi \neq 0$ in DCM, and $|\cos(\phi)|_{DCM} < 1$ can be derived from the equation sets (43) and (45) for an efficient solution to ϕ. Otherwise, if operation reaches a CCM range when changing frequency, then $|\cos(\phi)|_{CCM} \geq 1$ exists when solving the equation sets (43) and (45) with the initial assumption that the operation is in DCM. In such a case, there is no solution to ϕ, or $\phi = 0$ exists, so it is necessary to return to the derivations of Section IV-A for CCM analysis. The flow chart for identification of the operation mode and derivation of power factor and output power is shown in Fig. 6.

D. Extension to Other Topologies

The analysis algorithm proposed in this paper for the exploration of ac output power factor characteristics and voltage phase difference relationships of the studied topology could be readily extended to other common WPT topologies. First, the integrated LCC compensation topology can be transformed into other simple ones. For instance, it changes to an SS resonant topology as long as the following condition is given: $L_{f1} = L_{f2} = M_1 = M_2 = C_{f1} = C_{f2} = 0$. Accordingly, the derivation equations in this paper could all be simplified to match the SS resonant topology. Second, the proposed analysis using Fourier transform and FHA is also suitable for solving similar problems of other WPT systems.

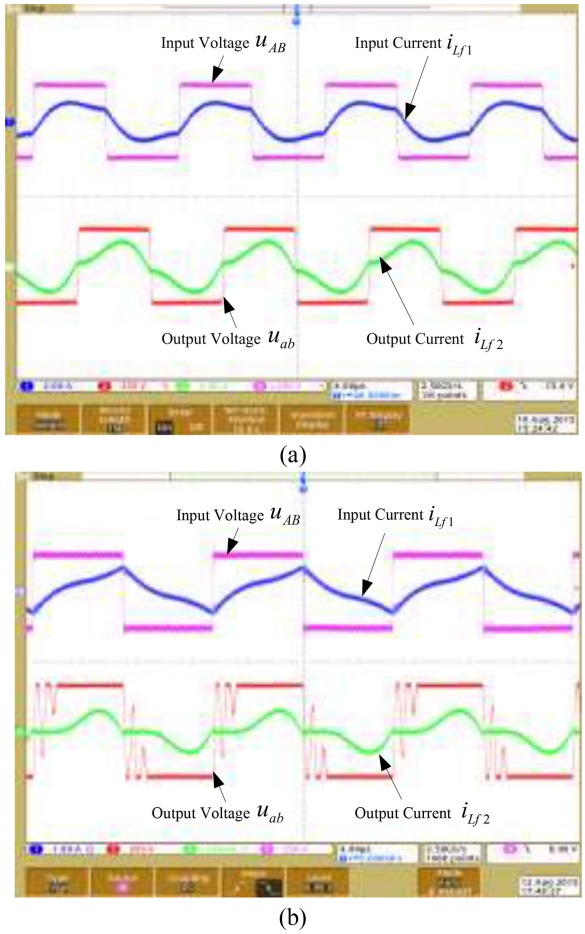

Fig. 8. Experimental waveforms of input and output voltages and currents. (a) CCM at 96 kHz. (b) DCM at 77 kHz.

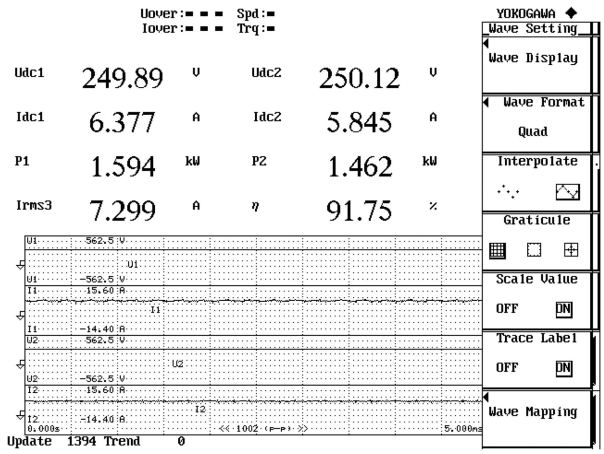

Fig. 9. Capture of power analyzer at 96 kHz with no misalignment.

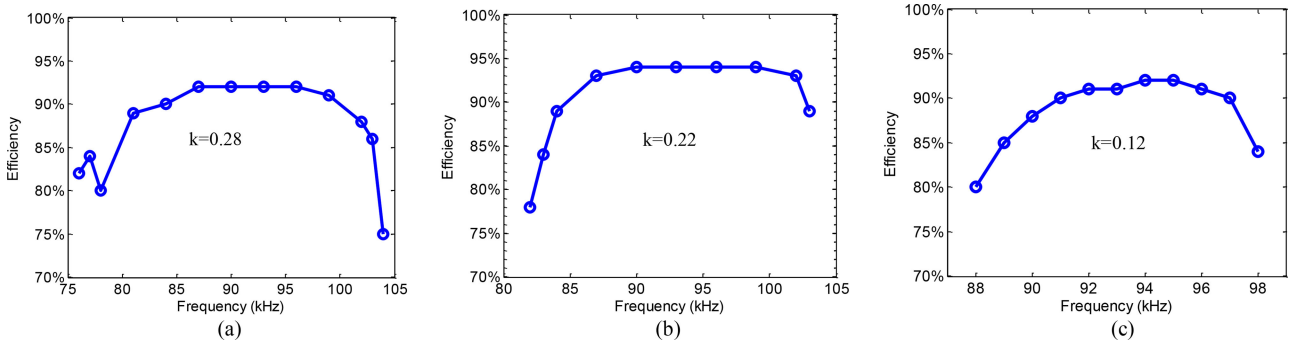

Fig. 10. Efficiencies of the WPT system at different frequencies. (a) $X = 0$ mm, $Y = 0$ mm. (b) $X = 200$ mm, $Y = 0$ mm. (c) $X = 0$ mm, $Y = 150$ mm.

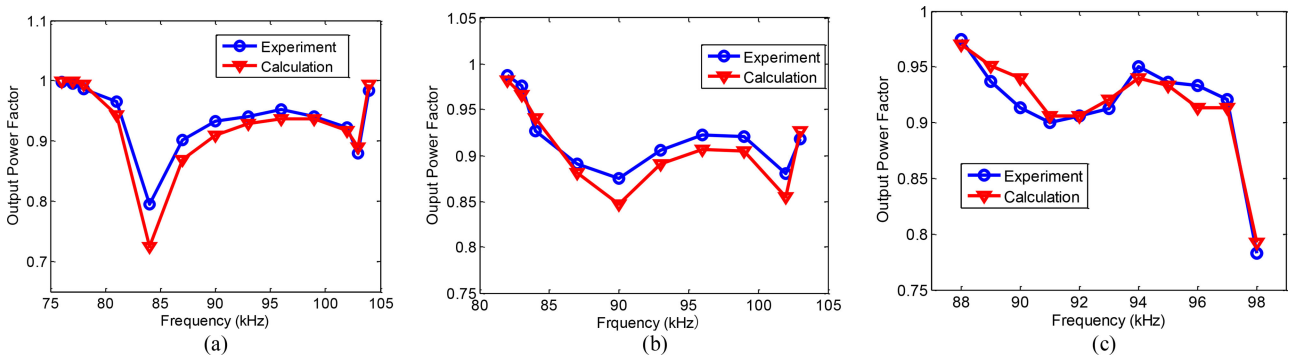

Fig. 11. Experimental and calculated ac output power factor of the WPT system at different frequencies. (a) $X = 0$ mm, $Y = 0$ mm. (b) $X = 200$ mm, $Y = 0$ mm. (c) $X = 0$ mm, $Y = 150$ mm.

V. Experimental Verification

The experimental setup for the integrated *LCC* compensation WPT system (see Fig. 7) is built to verify the proposed modeling and analysis of the ac output power factor and voltage phase relationships. A high power dc supply is used to emulate the input of the inverter and an electronic load is used to replace the battery. A controller is responsible for sending PWM signals to the inverter and receiving measured current or voltage signals from the WPT system. The *X*- or *Y*-misalignments of the coils could be adjusted as required. The specifications of the studied prototype are given in Table I.

The resonant frequency of the WPT system is calculated to be 96 kHz. The experimental input and output waveforms with no misalignment at two different switching frequencies (96 and 77 kHz) are shown in Fig. 8, typically indicating the CCM and DCM, respectively. It can be seen from Fig. 8 (a) that the output ac voltage has obvious oscillation in stage O, which results from the diode reverse recovery current and nonignorable i_{Lf2} slope (although i_{Lf2} remains nearly zero in stage O).

A Yokogawa power analyzer, WT1600, is employed to measure the input dc power supply power and output electronic load power, and then, to calculate the efficiency of the WPT system. A capture of the power analyzer at 96 kHz with no misalignment is shown in Fig. 9. Three cases are defined: Case I, there is no *X*- or *Y*-misalignment; Case II, *X*-misalignment equals 200 mm, and there is no *Y*-misalignment; Case III, *Y*-misalignment equals 150 mm, and there is no *X*-misalignment. The coupling coefficients in Cases I–III are 0.28, 0.22, and 0.13, respectively. As can be seen in Fig. 10, high efficiencies usually appear around the resonant frequency, and the highest efficiency of 94.31% is achieved at 96 kHz in Case II.

To validate the correctness of the calculation in Section IV for CCM and DCM, the experimental and calculated results are compared. It is noted that the experimental results (e.g., power factor, phase, etc.) are not directly measured, but derived from the saved waveform data of the oscilloscope. MATLAB as a mathematical tool is used for FHA and amplitude/phase acquisition at the fundamental frequency. According to the mathematical analysis in Section IV, the CCM intervals of operating frequencies for Cases I and II can be calculated as [83.8 kHz, 103.2 kHz] and [89.5 kHz, 102.1 kHz], respectively, otherwise the operation modes are DCM for the two cases. The operation modes for various operating frequencies in Case III are all DCM. The ac power factors in the aforementioned three cases are given in Fig. 11. Evidently, the power factors at some frequencies are not units at all, and meanwhile, the calculations match the experimental results well, which verifies that the proposed analysis of the ac power factor for CCM and DCM is correct. It is also observed that the power factor is nearly unity at low operating frequencies. The explanation is given as follows. The effective square output voltage interval where the current is not zero is getting thinner when the operating frequency or output power decreases in DCM. Meanwhile the output current has less distortions when it is effective or in other words it is not zero. The phase difference between the output voltage and current after the Fourier Transform becomes smaller accordingly, resulting

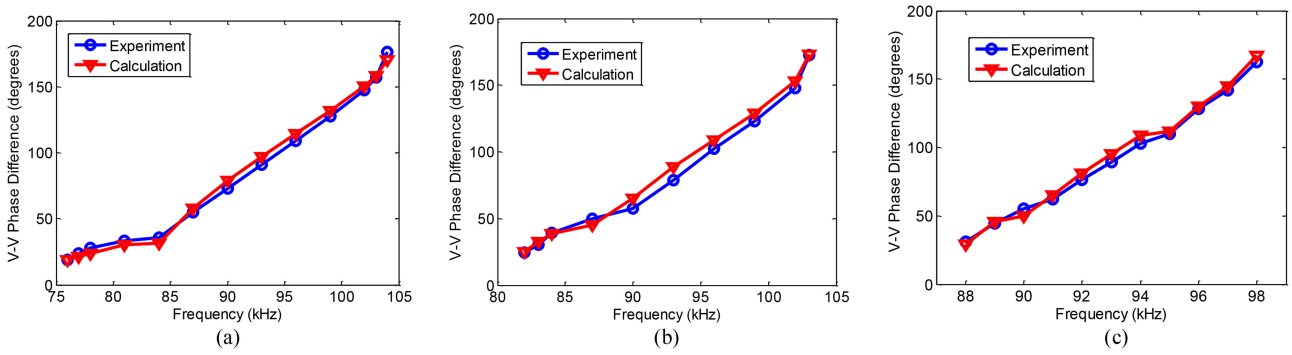

Fig. 12. Experimental and calculated phase differences between input and output voltages of the WPT system at different frequencies. (a) $X = 0$ mm, $Y = 0$ mm. (b) $X = 200$ mm, $Y = 0$ mm. (c) $X = 0$ mm, $Y = 150$ mm.

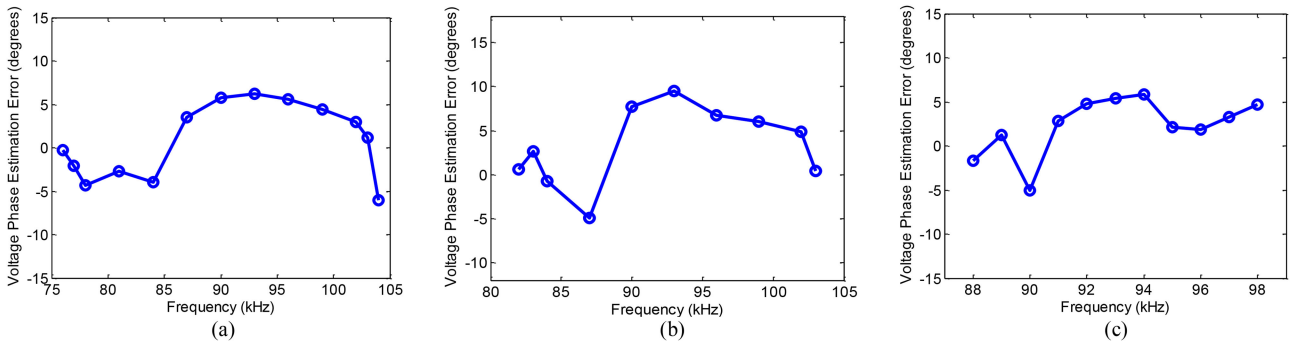

Fig. 13. Estimation errors between experimental and calculated results of input and output voltage phase difference at various frequencies. (a) $X = 0$ mm, $Y = 0$ mm. (b) $X = 200$ mm, $Y = 0$ mm. (c) $X = 0$ mm, $Y = 150$ mm.

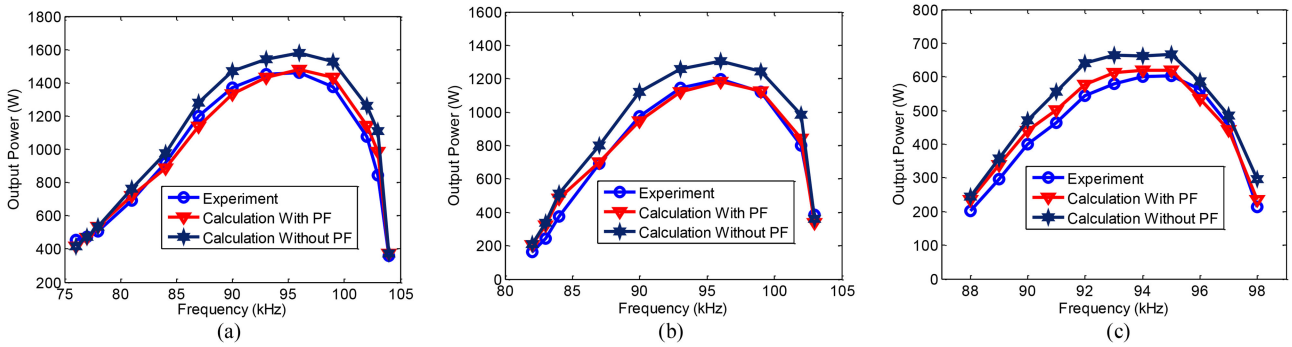

Fig. 14. Experimental and calculated output power of the WPT system at different frequencies. (a) $X = 0$ mm, $Y = 0$ mm. (b) $X = 200$ mm, $Y = 0$ mm. (c) $X = 0$ mm, $Y = 150$ mm.

in increase of the power factor. In extreme situations, the power factor is nearly unity. The experimental and calculated phase differences between the input and output voltages are compared in Fig. 12, and the corresponding estimation errors between the experimental and calculated results are shown in Fig. 13. It is observed that the phase difference goes up with the increase of the switching frequency in all three cases, and the calculations are very close to the experimental results.

The output power is depicted in Fig. 14, which gives a comparison between experimental results and calculations with/without power factor introduction. The calculated output power is derived from equations (34), (35), (58), and (59) with consideration of losses from an uncontrolled rectifier. To calculate the output power without power factor is also dependent on these equations where the power factor is set to 1 and rectifier losses are considered too. The output power, without power factor consideration, is much higher than that of experiments and calculations with power factors, while the latter two are very close to each other. Thus, it is essential not to ignore the output ac power factor. Additionally, precise calculation/estimation of output power in

the WPT system is important to topology design and realization of some control strategies, e.g., feedforward control, model prediction control, etc.

VI. Conclusion

In this paper, the exploration of the ac power factor characteristics and voltage phase relationships in wireless chargers of EVs is proposed, in order to correct a common misunderstanding that the ac output power factor of a WPT system is always unity. The CCM and DCM with various frequencies are discussed, covering expected operation conditions. An equivalent output voltage curve is introduced to decrease the calculation complexity in DCM. With simple transformation, the presented methodology for an integrated *LCC* compensation topology can be readily extended to other WPT systems. It also contributes the new topology design and realization of some control strategies with precise power calculation/estimation required. The comparison of experimental and calculated results proves the correctness and validity of the proposed strategy.

References

[1] M. A. Delucchi, C. Yang, A. F. Burke, J. M. Ogden, K. Kurani, J. Kessler, and D. Sperling, "An assessment of electric vehicles: Technology, infrastructure requirements, greenhouse-gas emissions, petroleum use, material use, lifetime cost, consumer acceptance and policy initiatives," *Philos. Trans. Roy. Soc. A, Math. Phys. Eng. Sci.*, vol. 372, no. 2006, pp. 325–351, Jan. 2014.

[2] J. Seixas, S. Simoes, L. Dias, A. Kanudia, P. Fortes, and M. Gargiulo, "Assessing the cost-effectiveness of electric vehicles in European countries using integrated modeling," *Energy Policy*, vol. 80, pp. 165–176, May 2015.

[3] M. Ettorre and A. Grbic, "A transponder-based, nonradiative wireless power transfer," *IEEE Antennas Wireless Propag. Lett*., vol. 11, pp. 1150–1153, Oct. 2012.

[4] L. Xie, Y. Shi, Y. T. Hou, and A. Loiu, "Wireless power transfer and applications to sensor networks," *IEEE Wireless Commun.*, vol. 20, no. 4, pp. 140–145, Aug. 2013.

[5] K. Ghate and L. Dole, "A review on magnetic resonance based wireless power transfer system for electric vehicles," in *Proc. Int. Conf. Pervasive Comput.*, 2015, pp. 1–3.

[6] S. Kong, B. Bae, J. J. Kim, S. Kim, D. H. Jung, and J. Kim, "Electromagnetic radiated emissions from a repeating-coil wireless power transfer system using a resonant magnetic field coupling," in *Proc. IEEE Wireless Power Transf. Conf.*, 2014, pp. 138–141.

[7] W. Zhong and S. Y. R. Hui, "Auxiliary circuits for power flow control in multifrequency wireless power transfer systems with multiple receivers," *IEEE Trans. Power Electron.*, vol. 30, no. 10, pp. 5902–5910, Oct. 2015.

[8] K. Lee and D. H. Cho, "Diversity analysis of multiple transmitters in wireless power transfer system," *IEEE Trans. Magn.*, vol. 49, no. 6, pp. 2946–2952, Jun. 2013.

[9] D. Ahn and S. Hong, "Wireless power transfer resonance coupling amplification by load-modulation switching controller," *IEEE Trans. Ind. Electron.*, vol. 62, no. 2, pp. 898–909, Feb. 2015.

[10] R. Feng, Q. Li, Q. Zhang, and J. Qin, "Robust secure transmission in MISO simultaneous wireless information and power transfer system," *IEEE Trans. Veh. Technol.*, vol. 64, no. 1, pp. 400–405, Jan. 2015.

[11] N. Kuyvenhoven, C. Dean, J. Melton, J. Schwannecke, and A. E. Umenei, "Development of a foreign object detection and analysis method for wireless power systems," in *Proc. IEEE Symp. Product Compliance Eng.*, 2011, pp. 1–6

[12] S. Li and C. C. Mi, "Wireless power transfer for electric vehicle applications," *IEEE J. Emerg. Sel. Topics Power Electron.*, vol. 3, no. 1, pp. 4–17, Mar. 2015.

[13] Z. Zhang, K. T. Chau, C. Qiu, and C. Liu, "Energy encryption for wireless power transfer," *IEEE Trans. Power Electron.*, vol. 30, no. 9, pp. 5237–5246, Sep. 2015.

[14] W. Zhang, S. C. Wong, C. K. Tse, and Q. Chen, "Design for efficiency optimization and voltage controllability of series-series compensated inductive power transfer systems," *IEEE Trans. Power Electron.*, vol. 29, no. 1, pp. 191–200, Jan. 2014.

[15] C. S. Wang, G. A. Covic, and O. H. Stielau, "Power transfer capability and bifurcation phenomena of loosely coupled inductive power transfer systems," *IEEE Trans. Ind. Electron.*, vol. 51, no. 1, pp. 148–57, Feb. 2004.

[16] J. Kim, D. H. Kim, and Y. J. Park, "Analysis of capacitive impedance matching networks for simultaneous wireless power transfer to multiple devices," *IEEE Trans. Ind. Electron.*, vol. 62, no. 5, pp. 2807–2813, May 2015.

[17] B. Wang, A. P. Hu, and D. Budgett, "Maintaining middle zero voltage switching operation of parallel-parallel tuned wireless power transfer system under bifurcation," *IET Power Electron.*, vol. 7, no. 1, pp. 78–84, 2014.

[18] J. L. Villa, J. Sallan, J. F. Sanz Osorio, and A. Llombart, "High-misalignment tolerant compensation topology for ICPT systems," *IEEE Trans. Ind. Electron.*, vol. 59, no. 2, pp. 945–951, Feb. 2012.

[19] U. K. Madawala and D. J. Thrimawithana, "A bidirectional inductive power interface for electric vehicles in V2G systems," *IEEE Trans. Ind. Electron.*, vol. 58, no. 10, pp. 4789–4796, Oct. 2011.

[20] A. P. Hu, *Wireless/Contactless Power Supply:-Inductively Coupled Resonant Converter solutions*, Saarbrücken, Germany: VDM Publishing, 2009, pp. 139–141.

[21] W. Li, C. C. Mi, S. Li, J. Deng, T. Kan, and H. Zhao, "Integrated LCC compensation topology for wireless charger in electric and plug-in electric vehicles," *IEEE Trans. Ind. Electron.*, vol. 62, no. 7, pp. 4215–4225, Jul. 2015.

[22] D. J. Thrimawithana and U. K. Madawala, "A generalized steady-state model for bidirectional IPT systems," *IEEE Trans. Power Electron.*, vol. 28, no. 10, pp. 4681–4689, Oct. 2013.

[23] V. Agarwal, K. Uthaichana, R. A. Decarlo, L. H. Tsoukalas, "Development and validation of a battery model useful for discharging and charging power control and lifetime estimation," *IEEE Trans. Energy Convers.*, vol. 25, no. 3, pp. 821–835, Sep. 2010.

[24] I. S. Suh, M. Lee, J. Kim, S. T. Oh, and J. P. Won, "Design and experimental analysis of an efficient HVAC (heating, ventilation, air-conditioning) system on an electric bus with dynamic on-road wireless charging," *Energy*, vol. 81, pp. 262–273, Mar. 2015.

[25] A. Baumgardt, F. Bachheibl, and D. Gerling, "Utilization of the battery recovery effect in hybrid and electric vehicle applications," in *Proc. 17th Int. Conf. Electr. Mach. Syst.*, 2015, pp. 254–260.

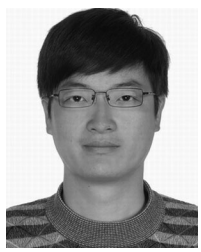

Xi Zhang (M'08–SM'13) received the B.Sc. degree in applied mathematics and the B.E. degree in information and control engineering, in 2002, and the M.E. and Ph.D. degrees in power electronics and electric power drive, in 2004 and 2007, respectively, all from Shanghai Jiao Tong University (SJTU), Shanghai, China.

From September 2007 to July 2009, he was a Postdoctoral Fellow with the Department of Electrical and Computer Engineering, University of Michigan-Dearborn, MI, USA. He is currently an Associate Professor with the Institute of Automotive Engineering and National Engineering Lab for Automotive Electronics and Control Technology, SJTU. His research interests include battery management systems, power electronics devices, and electric motor control systems for alternative-fuel vehicles.

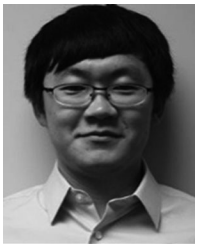

Tianze Kan (S'15) received the B.Eng. degree in electrical engineering and automation from the Huazhong University of Science and Technology, Wuhan, China, in 2011, and the M.S. degree in electrical engineering from the University of Southern California, Los Angeles, CA, USA, in 2013. He is currently working toward the Ph.D. degree in electrical and computer engineering in the joint doctoral program between San Diego State University and the University of California at San Diego, CA, USA.

His research interests include inductive-based wireless power transfer, especially on coil design and compensation topologies.

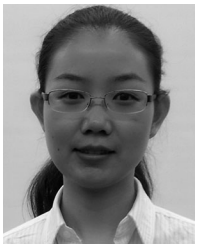

Chenwen You received the B.S. degree in electrical engineering and automation from the Huazhong University of Science and Technology, Wuhan, China, in 2010 and the M.S. degree in electrical engineering from the Electrical and Computer Engineering Department, University of Michigan-Dearborn, MI, USA. She is currently working toward the Ph.D. degree in electrical engineering from the Department of Electrical and Computer Engineering, San Diego State University, San Diego, CA, USA.

Her current research interests include power electronics, wireless charger, and power management in hybrid electric vehicles and hybrid energy storage system.

Chris Mi (S'00–A'01–M'01–SM'03–F'12) received the B.S.E.E. and M.S.E.E. degrees in electrical engineering from Northwestern Polytechnical University, Xi'an, China, in 1985 and 1988, respectively, and the Ph.D. degree in electrical engineering from the University of Toronto, Toronto, Canada, in 2000.

He is a Professor and Chair of Electrical and Computer Engineering and the Director of the Department of Energy funded Graduate Automotive Technology Education Center for Electric Drive Transportation, San Diego State University (SDSU), San Diego, CA, USA. Prior to joining SDSU, he was with with University of Michigan, Dearborn, MI, USA, from 2001 to 2015. He was the President and the Chief Technical Officer of 1Power Solutions, Inc. from 2008 to 2011. He is the Cofounder of Gannon Motors and Controls LLC and Mia Motors, Inc. His research interests include electric drives, power electronics, electric machines, renewable-energy systems, and electrical and hybrid vehicles. He has conducted extensive research and has published more than 100 journal papers. He has taught tutorials and seminars on the subject of HEVs/PHEVs for the Society of Automotive Engineers, the IEEE, workshops sponsored by the National Science Foundation, and the National Society of Professional Engineers. He has delivered courses to major automotive OEMs and suppliers, including GM, Ford, Chrysler, Honda, Hyundai, Tyco Electronics, A&D Technology, Johnson Controls, Quantum Technology, Delphi, and the European Ph.D. School. He has offered tutorials in many countries, including the U.S., China, Korea, Singapore, Italy, France, and Mexico. He has published more than 100 articles and delivered 30 invited talks and keynote speeches. He has also served as a panelist in major IEEE and SAE conferences.

Dr. Mi received the "Distinguished Teaching Award" and "Distinguished Research Award" of the University of Michigan Dearborn. He received the 2007 IEEE Region 4 "Outstanding Engineer Award," "IEEE Southeastern Michigan Section Outstanding Professional Award," and the SAE Environmental Excellence in Transportation (E2T).